Numerical simulation of electrovortex flows in cylindrical fluid layers and liquid metal batteries

Herreman, W.; Nore, C.; Ziebell Ramos, P.; Cappanera, L.; Guermond, J.-L.; Weber, N.;

Originally published:

November 2019

Physical Review Fluids 4(2019), 113702

DOI: https://doi.org/10.1103/PhysRevFluids.4.113702

Numerical simulation of electro-vortex flows in cylindrical fluid layers and liquid metal batteries

W. Herreman,* C. Nore, and P. Ziebell Ramos
Laboratoire d'Informatique pour la Mécanique et les Sciences de l'Ingénieur, LIMSI, CNRS, Univ. Paris-Sud, Université Paris-Saclay, Bât 507, Campus Universitaire F-91405 Orsay

L. Cappanera
Department of Computational and Applied Mathematics, Rice University, 6100 Main MS-134 Houston, TX 77005, USA

J.-L. Guermond
Department of Mathematics, Texas A&M University 3368 TAMU, College Station, TX 77843-3368, USA

N. Weber
Helmholtz-Zentrum Dresden - Rossendorf, Bautzner Landstr. 400, 01328 Dresden, Germany
(Dated: July 19, 2019)

We use the multiphase magnetohydrodynamic code SFEMaNS to study the generation of electro-vortex flows in liquid metal batteries. We first reproduce some well known results in a single-phase liquid metal column and then we characterize the electro-vortex flow in layered multiphase fluid systems. A simple energy density balance argument accurately estimates the typical interface deformation caused by the electro-vortex flow. When applied to Mg-Sb liquid metal batteries, we find that the electro-vortex flows may have the capacity to cause short-circuits even in moderate size batteries with radii in the range $[10, 20]$ cm.

PACS numbers: 47.65.-d, 52.65.Kj

I. INTRODUCTION

Intermittent electrical energy sources, such as wind and solar energy cannot have a significant impact on the global energy budget unless inexpensive and large scale storage devices are put in place. Amongst the various options that are currently studied, liquid metal batteries (LMBs) have been identified to be viable candidates [1–3]. In this article, we study how the magnetohydrodynamic phenomenon known as electro-vortex flow can impact the stably stratified structure of LMBs.

A sketch of a typical LMB configuration is shown in Figure 1-(a). A light liquid metal (represented with the letter A) is positioned on top of a medium density electrolyte composed of molten salt, itself on top of a heavy liquid metal alloy that has a high affinity for A (represented by the symbols B(A)). During discharge, electrons flow through the external circuit, while elements A dissolve as ions A^+ at the top of the electrolyte layer. At the bottom of the electrolyte, ions A^+ leave the electrolyte and alloy with B. As a result, the top layer of the LMB gets thinner and the bottom layer gets thicker during discharge. During charge the opposite mechanisms take place and the cell is restored to its original configuration. LMBs have attractive properties (low cost materials, high energy-efficiency, high capacity retention, and high cyclability), but heir main drawback is that they need to be heated ($\sim 400\,^\circ$C) to remain liquid. This certainly has an energetic cost, but not one that is prohibitive. Over the recent years, small LMB prototypes using inexpensive and Earth abundant materials have been built and tested [1–3]. The technology is presently being upscaled to allow a first phase of commercialization, but further studies are needed to reveal the full possibilities and limitations of the LMB technology.

The design of new LMB prototypes is necessary, but it is also interesting to use numerical simulations as a complementary tool to get insights in the chemical and physical processes occuring inside these cells. Fluid motions, of hydrodynamical, thermal or magnetohydrodynamical origin are unavoidable in LMBs and have received a particular attention (natural convection [4–8], the Tayler instability [9–11], the metal pad roll instability [12–19], and the electro-vortex flow [4, 7, 10, 20]). Too intense flows need to be avoided as they can compromise the stable stratification of the battery. On the other hand, flows can also be desirable. In the alloy layer, flows will improve the mixing limiting mass

*Electronic address: wietze.herreman@limsi.fr

transfer overpotentials [2, 4] or the formation of undesirable (solid) inter-metallic phases. We refer the reader to [9] where safety issues connected to magnetohydrodynamic instabilities are discussed and to [21] for a recent review of flows in LMBs.

In this article, we continue this research of fluid flows in LMBs, focussing on the so-called electro-vortex flow (EVF). EVF commonly arises in liquid metals regions that are in contact with thinner solid electrodes; see [22] for a detailed overview. Due to a difference in shape between the solid electrode and the liquid metal bath, the field lines of the electrical current $\boldsymbol{j}$ spread out as sketched in Figure 1-(b). Along with this current comes a magnetic induction $\boldsymbol{b}$ and a Lorentz-force $\boldsymbol{j}\times\boldsymbol{b}$ that effectively pushes the liquid metal away from the solid electrodes towards less intense $\boldsymbol{j}$ regions, see [23]. Inside a LMB, strong enough EVF can deform the interfaces separating the fluid layers and potentially even cause short-circuits, see Figure 1-(c). The objective of this paper is to characterize the intensity of the EVF inside multiphase systems, such as a LMBs and to asses whether EVF may cause short-circuits. The investigation is done numerically by using the massively parallel, multiphase, magnetohydrodynamic code SFEMaNS (the acronym stands for Spectral/Finite Element code for Maxwell and Navier-Stokes equations). This code uses cylindrical coordinates and is well suited to study the EVF in axisymmetric domains. Full details on the numerical method that is used are given in [24]. The multiphase algorithm in SFEMaNS has been benchmarked with OpenFOAM on the metal pad roll problem in [19]. Some supplementary elements regarding the numerical method are provided in Appendix A.

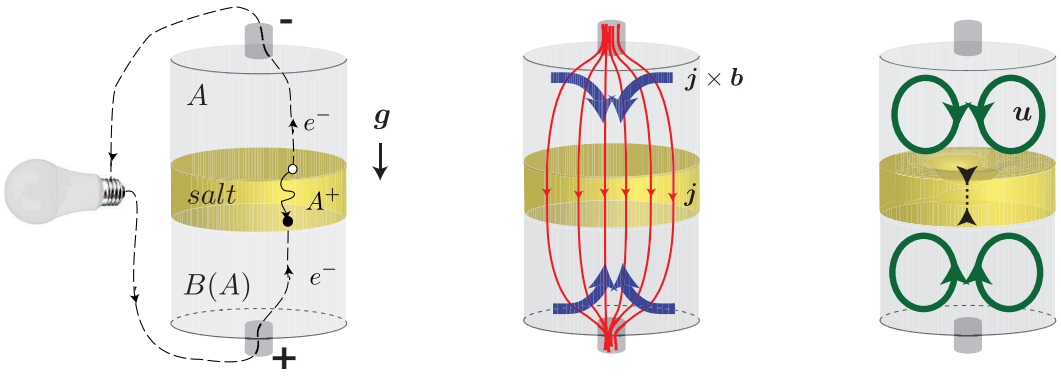

(a) (b) (c)

FIG. 1: A liquid metal battery (LMB) is composed of 3 layers of superposed conducting fluids with different densities. During discharge (a), electrons pass from the $-$ to the $+$ pole in the external circuit. Inside the battery, the top metal A dissolves as ions A^+ migrate downwards in the electrolyte, and ultimately alloy with the bottom metal $B(A)$. (b) The shape of the current collectors causes the field lines of the electrical current $\boldsymbol{j}$ to spread out as they enter the top and the bottom layers. This causes an azimuthal magnetic field $\boldsymbol{b}$ and an inward Lorentz-force $\boldsymbol{j}\times\boldsymbol{b}$. As a result an electro-vortex flow $\boldsymbol{u}$ is created in both the top and the bottom layers, and this flow can deform the interfaces (c).

The article is structured as follows. In §II, we first study the EVF in a single fluid layer, to recover some well-known results and scaling laws in axisymmetric context and how this holds in three-dimensional simulations. We also investigate how a realistic solid electrode affects EVF and this allows to discuss the accuracy of commonly used idealized boundary conditions (see [22, 25]). In §III, we study the EVF in setups composed of two and three layers of conducting fluids and in particular, the Mg-Sb LMB [1]. We calculate typical flow intensities and estimate the amplitude of the deformation of the interfaces caused by EVF. Using similitude principles, we then estimate typical battery sizes for which the EVF mechanism may become very intense and thereby compromise the stratified structure of the battery.

II. ELECTRO-VORTEX FLOW IN A SINGLE FLUID LAYER

A. Geometry and equations

We consider an incompressible liquid metal with kinematic viscosity ν and density ρ. The fluid domain is a cylinder of radius R and height H. The total electrical current I runs vertically through the system. This current enters at the bottom and is connected to the fluid through a section of radius R_w. The current exits at the top across the entire section of radius R. The chosen geometry is one of the classical examples of electro-vortex flow investigated in

the literature, theoretically [25–28], numerically [29–31], and experimentally [32, 33].

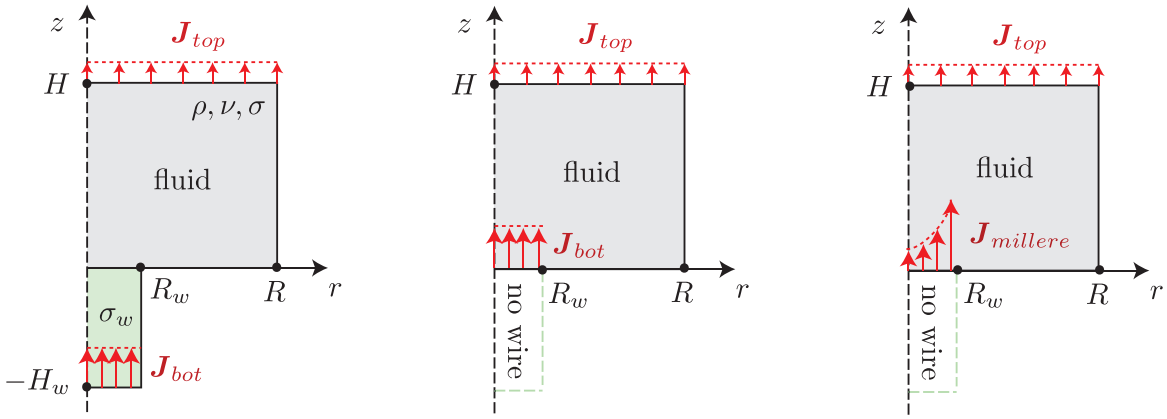

(a) wire (b) uniform (c) Millere

FIG. 2: Computational domains used to study the EVF in a liquid metal column. On top of the fluid domain, we suppose a homogeneous current density $\boldsymbol{J}_{\text{top}}$. Three different setups are compared. In the setup (a), the fluid is connected electrically to a solid wire which is fed from below with a homogeneous current density $\boldsymbol{J}_{\text{bot}}$. In (b), there is no wire and a homogeneous current density $\boldsymbol{J}_{\text{bot}}$ directly enters the fluid domain. In (c), the wire is modeled by using a particular Millere current density profile (see Eq. (1)) over the section where the wire should be connected to the liquid bath.

We study three different setups sketched in Figure 2. In all the setups we suppose that the current density on the top section is homogeneous, $\boldsymbol{J}_{\text{top}} = (I/\pi R^2)\boldsymbol{e}_z$. In the setup (a), the fluid is electrically connected to a solid wire of height H_w and conductivity σ_w which is fed from below with a uniform current density $\boldsymbol{J}_{\text{bot}} = (I/\pi R_w^2)\boldsymbol{e}_z$. In the setup (b), referred to as the uniform case, there is no wire and a homogeneous current density $\boldsymbol{J}_{\text{bot}}$ directly enters the fluid domain. In the setup (c), referred to as the Millere case, there is no wire either, but, using cylindrical coordinates, we suppose that the current distribution has the following form:

$$\boldsymbol{J}_{\text{Millere}} = \frac{I}{2\pi R_w^2} \frac{1}{\sqrt{1-(r/R_w)^2}} \boldsymbol{e}_z \tag{1}$$

and enters through the cylindrical section $\{0 \leq r \leq R_w\}$. This particular current density profile has been used in [22, 25]; it corresponds to the current density that would be observed at the surface of a flat, perfectly conducting electrode of radius R_w, feeding a current I to a semi-infinite conductor. We expect that this distribution is a reasonable approximation for a thin well-conducting wire connected to a large fluid domain, i.e., when $\sigma_w \gg \sigma, R_w \ll R, R_w \ll H$.

We non-dimensionalize the problem using the following scales for space, time, velocity, pressure, and magnetic field:

$$[\boldsymbol{r}] = R, \quad [t] = \frac{R^2}{\nu}, \quad [\boldsymbol{u}] = \frac{\nu}{R}, \quad [p] = \frac{\rho\nu^2}{R^2}, \quad [\boldsymbol{b}] = \frac{\mu_0 I}{2\pi R}, \tag{2}$$

with μ_0 the magnetic permeability of vacuum. For brevity, we abuse the notation by not changing the notation for the non-dimensional variables, e.g. (r, θ, z) designate the non-dimensionalized, cylindrical coordinates. Three geometric non-dimensional parameters are fixed:

$$h = \frac{H}{R} = 1, \quad h_w = \frac{H_w}{R} = 1, \quad r_w = \frac{R_w}{R} = 0.2. \tag{3}$$

The following three remaining non-dimensional parameters are allowed to vary:

$$S = \frac{\mu_0 I^2}{4\pi^2 \rho \nu^2}, \quad P_m = \sigma \mu_0 \nu, \quad \hat{\sigma} = \frac{\sigma_w}{\sigma}. \tag{4}$$

The number S measures the ratio between the magnetic and the viscous forces and is referred to as the EVF parameter in [7]. P_m is the magnetic Prandtl number of the fluid. $\hat{\sigma}$ is the ratio of electrical conductivities of the wire and the fluid. The non-dimensional magnetohydrodynamic equations to be satisfied in the fluid are:

$$\partial_t \boldsymbol{u} + (\boldsymbol{u}\cdot\nabla)\boldsymbol{u} = -\boldsymbol{\nabla} p + \Delta \boldsymbol{u} + S(\boldsymbol{\nabla}\times\boldsymbol{b})\times\boldsymbol{b}, \tag{5a}$$

$$\partial_t \boldsymbol{b} = \boldsymbol{\nabla}\times(\boldsymbol{u}\times\boldsymbol{b}) + {P_\text{m}}^{-1}\Delta\boldsymbol{b}, \tag{5b}$$

$$\boldsymbol{\nabla}\cdot\boldsymbol{u} = 0, \tag{5c}$$

$$\boldsymbol{\nabla}\cdot\boldsymbol{b} = 0. \tag{5d}$$

Moreover, in the setup (a) described in Figure 2 we solve the induction equation in the wire

$$\partial_t \boldsymbol{b}_w = (\hat{\sigma} P_\mathrm{m})^{-1} \Delta \boldsymbol{b}_w, \tag{6a}$$
$$\boldsymbol{\nabla}\cdot\boldsymbol{b}_w = 0. \tag{6b}$$

At occasions we will use the notation $\boldsymbol{j} := \boldsymbol{\nabla}\times\boldsymbol{b}$, $\boldsymbol{j}_w := \boldsymbol{\nabla}\times\boldsymbol{b}_w$ for the electrical current densities in the fluid and in the wire, respectively. On the boundaries of the fluid domain we enforce the no-slip condition:

$$\boldsymbol{u}|_{r=1} = \boldsymbol{u}|_{z=1} = \boldsymbol{u}|_{z=0} = \boldsymbol{0}. \tag{7}$$

For the magnetic boundary conditions, we estimate the azimuthal component of the magnetic field at the radius r_b by using Ampère's law:

$$b_\theta|_{r=r_b} = \frac{1}{r_b}\int_0^{r_b} j_z r\,\mathrm{d}r. \tag{8}$$

We further assume that the other tangential component of the magnetic field (b_r on horizontal plates, b_z on lateral surfaces) vanishes. This yields the following set of boundary conditions for the fluid domain,

$$b_z|_{r=1} = 0, \quad b_\theta|_{r=1} = 1, \quad \forall z \in [0,1], \tag{9a}$$
$$b_r|_{z=h} = 0, \quad b_\theta|_{z=h} = r, \quad \forall r \in [0,1], \tag{9b}$$
$$b_r|_{z=0} = 0, \quad b_\theta|_{z=0} = 1/r, \quad \forall r \in [r_w,1], \tag{9c}$$

and depending on the setup

$$\begin{aligned}\text{(a) wire}: \quad & \boldsymbol{e}_z\times(\boldsymbol{b}-\boldsymbol{b}_w)|_{z=0} = 0, \quad \boldsymbol{e}_z\times(\boldsymbol{j}-(\boldsymbol{j}_w/\hat{\sigma}))|_{z=0} = 0, \quad \forall r\in[0,r_w],\\ & b_{w,z}|_{r=r_w} = 0, \quad b_{w,\theta}|_{r=r_w} = 1/r_w, \quad \forall z\in[-h_w,0],\\ & b_{w,r}|_{z=-h_w} = 0, \quad b_{w,\theta}|_{z=-h_w} = r/r_w^2, \quad \forall r\in[0,r_w],\end{aligned} \tag{10a}$$

$$\text{(b) uniform}: \quad b_r|_{z=0} = 0, \quad b_\theta|_{z=0} = r/r_w^2, \quad \forall r\in[0,r_w], \tag{10b}$$

$$\text{(c) Millere}: \quad b_r|_{z=0} = 0, \quad b_\theta|_{z=0} = \left(1-\sqrt{1-(r/r_w)^2}\right)/r, \quad \forall r\in[0,r_w]. \tag{10c}$$

In the setup (a), the above conditions enforce the continuity of the tangential magnetic and tangential electrical fields at the wire-fluid interface. The boundary condition in the setup (c) is obtained by using (1) in (8).

The Millere condition is often given in the literature in the form (10c); it is rarely formulated in the form (1). This condition is obtained by solving $\nabla\times\nabla\times(b_\theta\boldsymbol{e}_\theta) = -\Delta(b_\theta\boldsymbol{e}_\theta) = \boldsymbol{0}$ in oblate spheroidal coordinates in an infinite fluid domain above a perfectly conducting disk (see [22] for details). One then derives (10c) by expressing the solution thus obtained on the surface of the disk using cylindrical coordinates. Notice that, unlike the Millere current density, the Millere azimuthal magnetic field profile is not singular at $r = r_w$.

B. Axisymmetric study

In this section, we impose axisymmetry: all fields are θ-independent and $b_r = b_z = j_\theta = j_{w,\theta} = u_\theta = 0$.

1. *Spatial structure of current density, Lorentz force and electro-vortex flow*

As a first example, we focus on the setup with a wire that has the same conductivity as the liquid metal, $\hat{\sigma} = 1$ and further fix $P_\mathrm{m} = 0.2$, $S = 250$. Starting with the fluid at rest, a stationary flow is reached after a short transient. In Figure 3-(a) we show a collection of streamlines of the stationary electro-vortex flow in a meridional plane. A vertical jet directed away from the bottom electrode recirculates along the lateral wall. The flow is the most intense on the axis. Figure 3-(b) shows how the electrical current density spreads out from the bottom section to the top section. Panel (c) shows the field lines of the associated Lorentz-force. Notice that this force is very large close to the point $(r,z) = (0.2,0)$. When looking at this picture, it is not immediately clear how the Lorentz force can create the

electro-vortex flow. Actually only part of the Lorentz force contributes to the generation of the flow. Recalling that $b_r = b_z = 0$, we rewrite the Lorentz force as

$$\boldsymbol{j}\times\boldsymbol{b} = -\frac{b_\theta^2}{r}\,\boldsymbol{e}_r - \frac{1}{2}\boldsymbol{\nabla} b_\theta^2. \tag{11}$$

We thus separate a potential part $-\boldsymbol{\nabla} b_\theta^2/2$, which only modifies the pressure, from the quantity $-(b_\theta^2/r)\,\boldsymbol{e}_r$, which effectively drives the electro-vortex flow. The spatial distribution of $-(b_\theta^2/r)\,\boldsymbol{e}_r$ is shown in the panel (d) of Figure 3. Arrows (not at scale) suggest the radially inward direction and relative magnitude. This figure suggests better than Panel (c) that the fluid is being pushed towards the axis in the immediate vicinity of the bottom contact. It is the action of the force $-(b_\theta^2/r)\,\boldsymbol{e}_r$ combined with the incompressibility of the fluid that yields the fluid flow sketched in Figure 3-(a).

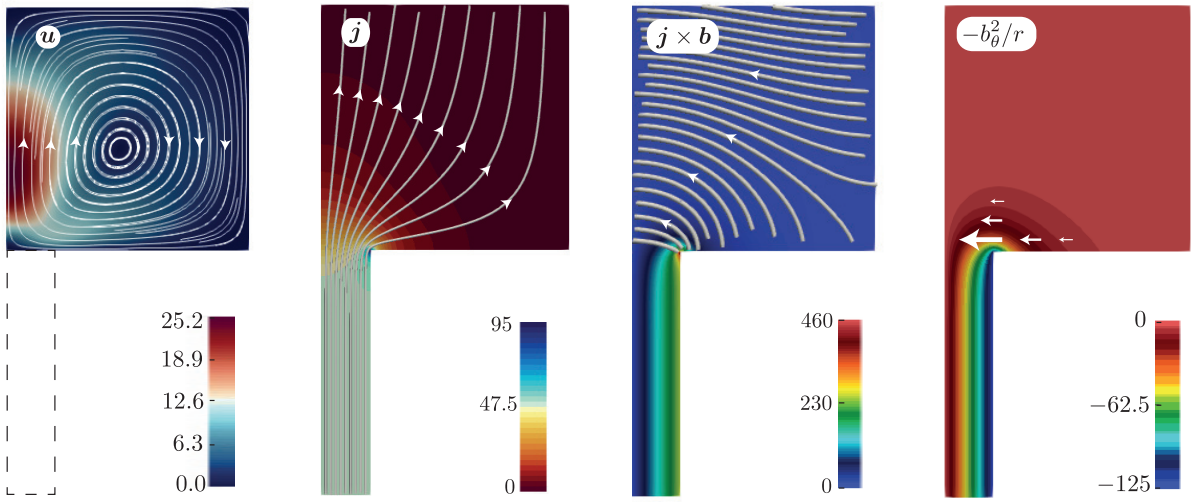

(a) (b) (c) (d)

FIG. 3: Steady state fields in the wire setup for $S = 250$, $P_\mathrm{m} = 0.2$, $\hat{\sigma} = 1$. (a) Electro-vortex flow and intensity in colorcode. (b) field lines and magnitude of the Electrical current density $\boldsymbol{j}$. (c) Lorentz-force $\boldsymbol{j}\times\boldsymbol{b}$ and intensity. Notice the concentration near $(r, z) = (0.2, 0)$. (d) Part of the Lorentz-force $-(b_\theta^2/r)\boldsymbol{e}_r$ that effectively drives the flow. Vectors suggest magnitude and direction but are not at scale.

2. *With or without wire*

Here we compare the setup (a) with wires of different conductivities $\hat{\sigma} = 0.01, 1, 56$ to the simplified models (b) and (c) without wire (uniform and Millere cases). We fix $S = 25$, $P_\mathrm{m} = 0.2$ in this section. In Figure 4-(a), we show the vertical flow $u_z(0, z)$ along the axis. All the curves have similar profiles. The uniform model yields the most intense flow, and we observe that it is well adapted to model the effect of a wire with low relative conductivity ($\hat{\sigma} \ll 1$). The Millere setup yields a less intense flow, and we observe that it is well adapted to model wires with high relative conductivity ($\hat{\sigma} \gg 1$). For wires with conductivities in the same range as the fluid ($\hat{\sigma} \approx 1$), the intensity of the flow is between that produced by the models (b) and (c). The Millere curve in Figure 4-(a) can be compared to the results provided in [22, p. 187]. Our results are not exactly identical but are qualitatively similar. To ascertain the accuracy of our computations, we show in Figure 4-(b) results with the Millere setup obtained on three different meshes. It seems clear that the results presented here are very close to convergence.

The relative conductivity of the wire has a strong impact on the vertical current density near the electrical contact. This is shown in Figure 5-(a): j_z evolves from an almost uniform profile in the case $\hat{\sigma} \ll 1$, towards the concentrated, Millere-like profile in the limit $\hat{\sigma} \gg 1$. Figure 5-(b) shows that, unlike j_z, b_θ is only weakly affected by $\hat{\sigma}$. Varying $\hat{\sigma}$, the field b_θ varies in the immediate neighborhood of the small wedge delimited by the Millere and uniform cases. Since b_θ is slightly more intense in the uniform setup (i.e., $\hat{\sigma} \ll 1$), and since the EVF is effectively forced by $-(b_\theta^2/r)\,\boldsymbol{e}_r$, we now understand why low values of $\hat{\sigma}$ yield slightly more intense EVF as observed in Figure 4-(a). Since the Lorentz force $\boldsymbol{j}\times\boldsymbol{b}$ is as sensitive to $\hat{\sigma}$ as j_z, its magnitude $\|\boldsymbol{j}\times\boldsymbol{b}\|$ can therefore reach very high values near the electrodes in

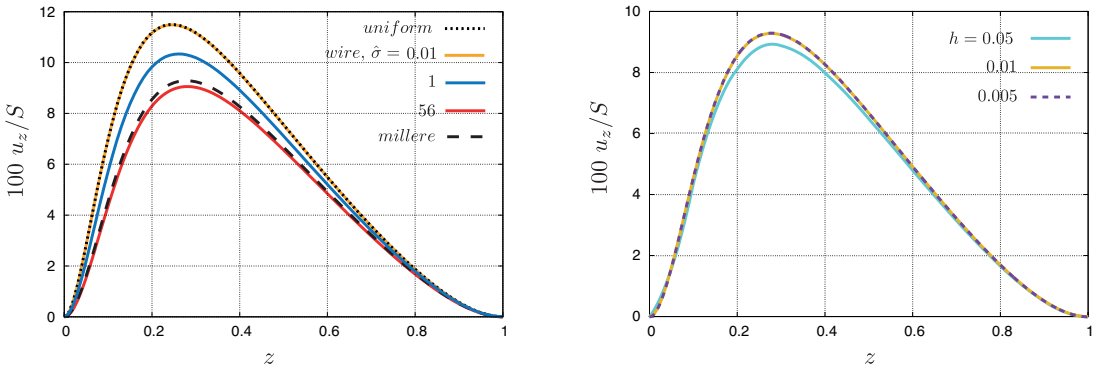

(a) (b)

FIG. 4: Vertical velocity on the axis $r = 0$ for the setups (a), (b), and (c), all obtained with $S = 25$, $P_\mathrm{m} = 0.2$. (a) At low wire conductivity ($\hat{\sigma} \ll 1$), the uniform current inlet model is well-adapted and the EVF the most intense. At high wire conductivity ($\hat{\sigma} \gg 1$), Millere's boundary condition is adequate and the EVF is the least intense. For $\hat{\sigma} \simeq 1$ the flow intensity ranges between those given by models (b) and (c). (b) Convergence study for the Millere setup, h is the typical mesh size.

the limit $\hat{\sigma} \gg 1$; this phenomenon is already visible in Figure 3-(c) for $\hat{\sigma} = 1$. Notice, however, that this singular behavior mainly affects the pressure in the fluid and not so much the intensity of the electro-vortex flow.

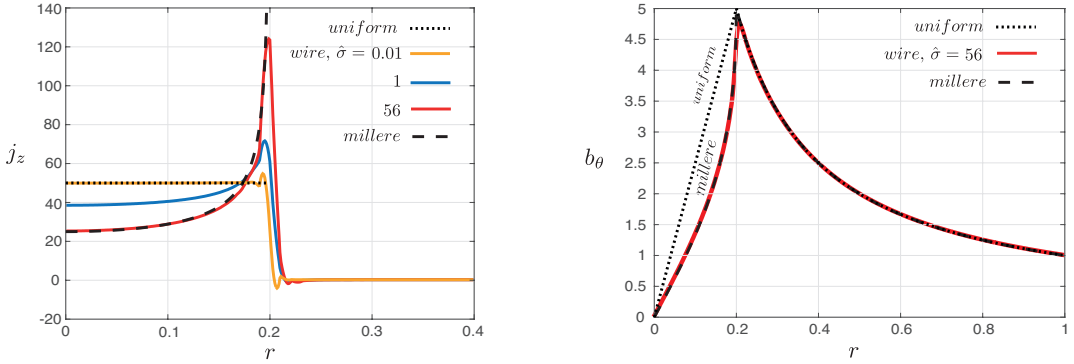

(a) (b)

FIG. 5: Current density j_z and azimuthal magnetic field b_θ at the bottom electrical contact $z = 0$ with or without wire ($S = 25$, $P_\mathrm{m} = 0.2$). (a) The current density j_z strongly depends on the conductivity of the wire. The (singular) Millere current density profile is adequate for high $\hat{\sigma} \gg 1$, the uniform current density is adequate for low $\hat{\sigma} \ll 1$. (b) The magnetic field b_θ is only weakly affected by $\hat{\sigma}$. The differences between the results obtained with the Millere and the uniform boundary conditions are small.

3. *Varying S*

We calculate the electro-vortex flow for various values of S in the range $[6.25, 5{\times}10^6]$ and with $P_\mathrm{m} \in \{0, 10^{-6}, 0.2\}$. We restrict ourselves to the Millere boundary condition in this section. We introduce a Reynolds number of the electro-vortex flow based on the maximal flow speed in the fluid. Given our choice of length and time scale, this number measures the flow intensity,

$$Re = \frac{U_\mathrm{max} R}{\nu} = \max_{\mathbf{x},t}(\|\boldsymbol{u}\|). \tag{12}$$

We show in Figure 6 the Reynolds number as a function of S in logarithmic scale (for the three values $P_\mathrm{m} \in \{0, 10^{-6}, 0.2\}$). We observe that Re (i.e., the flow intensity) monotonically increases with S. We observe that the flow at high values of S is weaker for $P_\mathrm{m} = 0.2$ than for $P_\mathrm{m} = 0$. For low values of P_m, we observe the following scaling laws:

$$\text{low } S \text{ range}: \quad Re \sim S \quad , \quad \text{high } S \text{ range}: \quad Re \sim S^{1/2}. \tag{13}$$

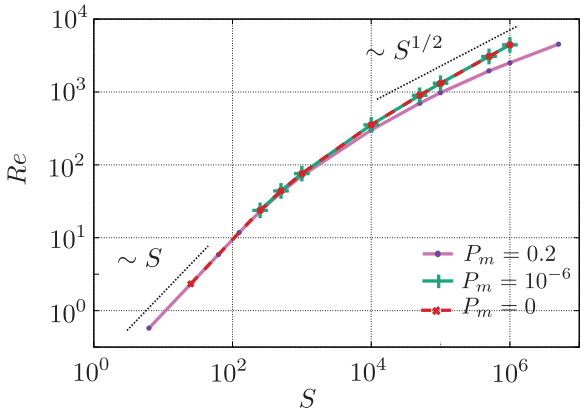

FIG. 6: Reynolds number of the electro-vortex flow based on the maximal speed, as a function of S and for various P_m. When S is small, we observe the scaling law $Re \sim S$ for all P_m. When S is large, we observe $Re \sim S^{1/2}$ for low values of P_m. Millere's boundary conditions are used at the current inlet.

These scaling laws when P_m is small are well known [22]. They can be inferred from the momentum eq. (5a). The force density $-(S\, b_\theta^2/r)\, \boldsymbol{e}_r$ which drives the EVF is proportional to S. Recalling that we are working with nondimensional equations, for low intensity flows, i.e., in the Stokes limit, this force is balanced by the viscous diffusion, $\|\Delta \boldsymbol{u}\| \sim S$, which yields $\|\boldsymbol{u}\| \sim S$ or $Re \sim S$. For high intensity flows, inertia takes over and we instead have $\|(\boldsymbol{u}\cdot\nabla)\boldsymbol{u}\| \sim S$ yielding $\|\boldsymbol{u}\| \sim \sqrt{S}$ or $Re \sim \sqrt{S}$. Bojarevics [22] proposed the following refinements of these scaling laws when P_m is small in order to take into account the size r_w of the wire:

$$Re = \begin{cases} S\,(10^{1+5r_w})^{-1/2} & \text{for } S < 10^3 \\ \sqrt{S}\,(10^{3-5r_w})^{1/3} & \text{for } S > 10^5. \end{cases} \tag{14}$$

Using $r_w = 0.2$, this gives $Re = 0.1{\times}S$ for $S < 10^3$, and $Re = 4.64{\times}S^{1/2}$ for $S > 10^5$. Let us compare these theoretical predictions to our numerical results, which we recall are all done with $r_w = 0.2$.

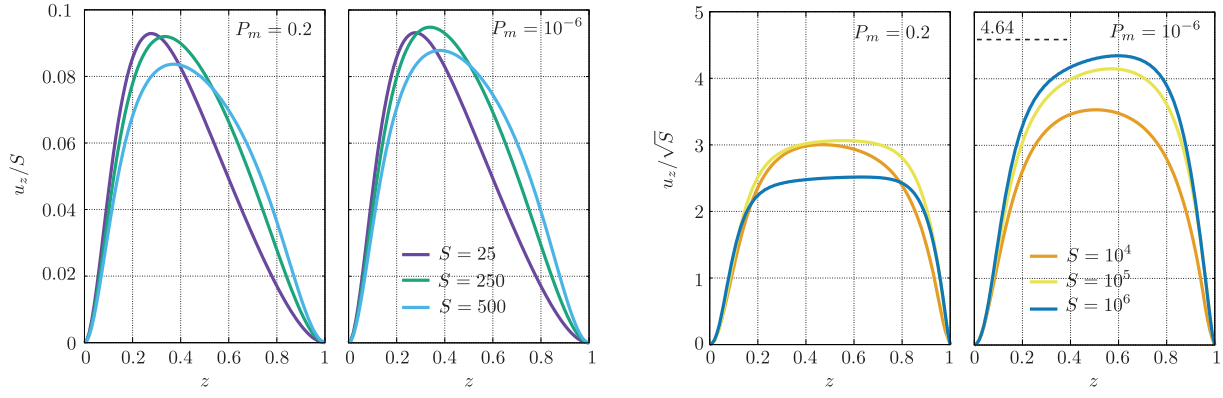

FIG. 7: Rescaled vertical velocity profiles along the axis $r = 0$, for various values of S and $P_\mathrm{m} \in \{10^{-6}, 0.2\}$ and using Millere boundary conditions. (a) In the low S range: velocity profiles rescale well as u_z/S for both values of P_m. (b) In the high S range: velocity profiles rescale well as $u_z/\sqrt{S}$.

In Figure 7 we display the vertical velocity along the axis ($r = 0$), rescaled by S in the low S regime (panel (a)) and rescaled by $S^{\frac{1}{2}}$ in the high S regime (panel (b)). In the low S regime, the law $Re \approx 0.1\, S$ is well adapted up to 4% for both low and high values of P_m. In the high S regime, we find that $Re \approx 4.64\ S^{1/2}$ is well adapted up to 3% for low values of P_m. Notice that spatial profiles of the velocity are different in the low S regime and in the high S regime. The maximum of the velocity profile is close to the wire when S is small, but the location of the maximum moves away from the wire as S increases.

The results shown in Figure 6 and in Figure 7 suggest that for high values of P_m and high values of S, the scaling law $Re \sim \sqrt{S}$ is no longer appropriate. This is due to inductive effects, i.e., the term $\nabla{\times}(\boldsymbol{u}{\times}\boldsymbol{b})$ reaches the same order of magnitude as the diffusive term ${P_\mathrm{m}}^{-1}\Delta\boldsymbol{b}$ when $Re \sim {P_\mathrm{m}}^{-1}$ or, alternatively, when the magnetic Reynolds

number $Rm = \sigma\mu_0 U_{\max} R$ is of order 1. In real liquid metals, where $P_{\rm m} \sim 10^{-6} - 10^{-7}$ is typical, inductive effects have very little impact unless S is extremely large.

Some further information on how the flow changes as S increases is given in Figure 8. We show streamlines and color maps of the magnitude of the velocity for $S \in \{500, 10^4, 5{\times}10^4, 5{\times}10^5\}$. The streamlines are rather symmetrical at low values of S, but symmetry breaks as S increases and we clearly see two phenomena happening when S is large. First, the fluid is ejected upwards so energetically that it hits the upper wall at right angle and gets violently ejected outwards in a thin layer that is almost as fast as the vertical jet. Second, the center of the main vortex moves towards the upper right corner, and the fluid in the bottom right corner becomes stagnant. The structure of the weak recirculation zone that appears in the bottom right corner around $S \sim 5{\times}10^4$ becomes gradually more complex as S increases.

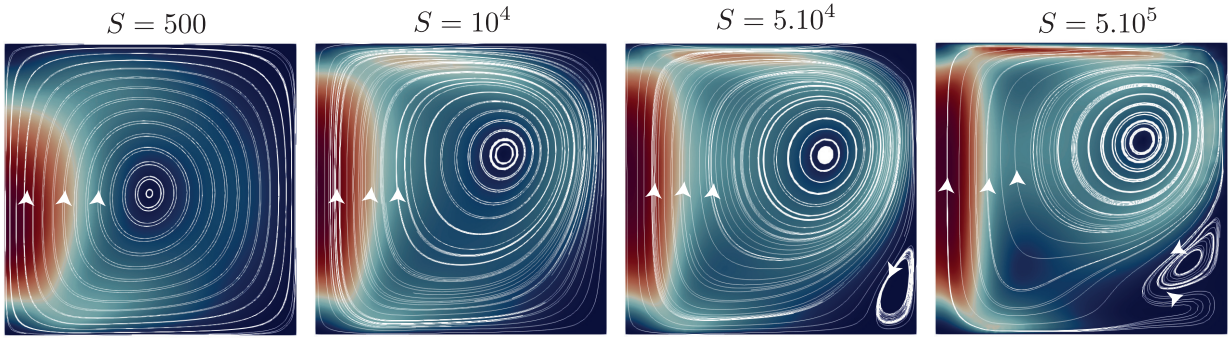

FIG. 8: Transition from viscous to inertial regime as S increases in axisymmetric computations. We show streamlines of the flow in meridional planes and the colors code the intensity. Millere boundary conditions, $P_m = 10^{-6}$ and $r_w = 0.2$.

C. Three-dimensional study

In this section we get rid of the axisymmetry assumption. Our goal is to find when the EVF becomes three-dimensional. All fields are spectrally decomposed in SFEMaNS. For instance the velocity has the following expression:

$$\boldsymbol{u} = \sum_{m=0}^{M-1} \boldsymbol{u}_m^c(r,z,t)\cos(m\theta) + \sum_{m=1}^{M-1} \boldsymbol{u}_m^s(r,z,t)\sin(m\theta), \tag{15}$$

where $\boldsymbol{u}_m^c(r,z,t)$ and $\boldsymbol{u}_m^s(r,z,t)$ are time-dependent quadratic finite element functions. After thorough investigations, we have observed that the azimuthal resolution $M = 16$ is sufficient for our study. In all the simulations that we have done we have observed that $u_{\theta,0} = 0$, i.e., there is no significant azimuthal axisymmetric flow.

In order to make diagnostics we calculate the total kinetic energy $K_{\rm tot}$, the part of the kinetic energy carried by the azimuthal flow component $K_{\rm tor}$, and the kinetic energy contained in the axisymmetric flow $K_{\rm axi}$. These quantities are defined by

$$K_{\rm tot} = \sum_{m=0}^{M-1}(1+\delta_{m0})\frac{\pi}{2}\int_0^1\int_0^1 \left(\|\boldsymbol{u}_m^c\|^2 + \|\boldsymbol{u}_m^s\|^2\right) r\,{\rm d}r\,{\rm d}z, \tag{16a}$$

$$K_{\rm tor} = \sum_{m=0}^{M-1}(1+\delta_{m0})\frac{\pi}{2}\int_0^1\int_0^1 \left(\|u_{\theta,m}^c\|^2 + \|u_{\theta,m}^s\|^2\right) r\,{\rm d}r\,{\rm d}z, \tag{16b}$$

$$K_{\rm axi} = \pi\int_0^1\int_0^1 \|\mathbf{u}_0^c\|^2\, r\,{\rm d}r\,{\rm d}z. \tag{16c}$$

The quantities $K_{\rm tor}$ and $K_{\rm tot} - K_{\rm axi}$ both provide simple measures of the three-dimensionality of the flow.

We have done a series of calculations in which we vary S in a configuration where a copper wire is connected to mercury ($\hat{\sigma} = 56$, $P_{\rm m} = 1.57{\times}10^{-7}$). All the calculations are started from the axisymmetric state. At low values of S, we observe that the electro-vortex flow remains axisymmetric and stationary. Beyond a critical value $S = S_c$, we observe a bifurcation towards a time-dependent three-dimensional motion. This is illustrated in Figure 9(a), where we show $K_{\rm tor}$ as a function of time. At $S = 7{\times}10^4$, $K_{\rm tor}$ decays exponentially, while for higher values of S, $K_{\rm tor}$ increases exponentially. We approximately locate the threshold of the three-dimensional instability at $S_c \approx 7.2{\times}10^4$.

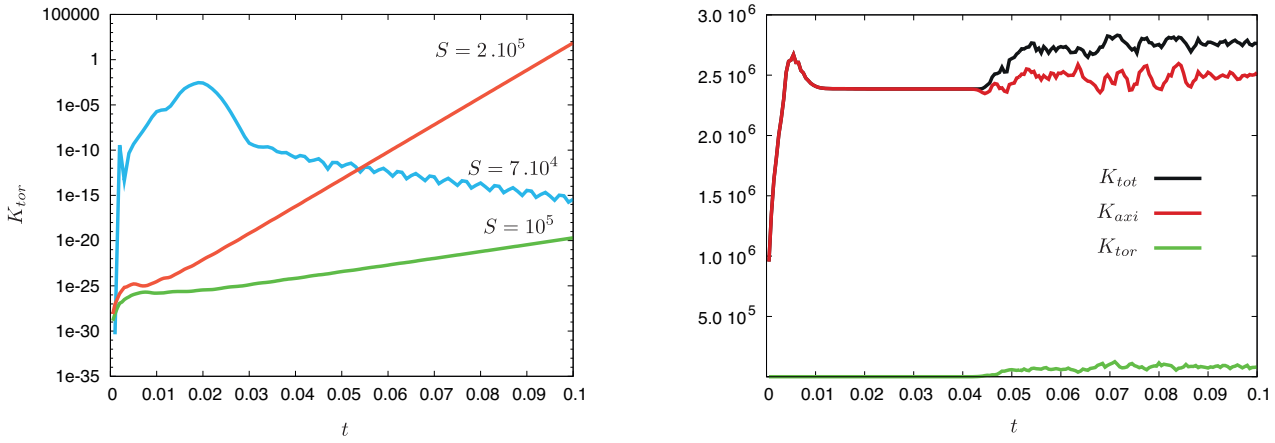

(a) (b)

FIG. 9: Time evolution of the kinetic energy measures $K_{\rm tot}, K_{\rm axi}, K_{\rm tor}$ (see (16a)-b-c) in three-dimensional electro-vortex flow simulations with wire, $\hat{\sigma} = 56$, $P_m = 1.57{\times}10^{-7}$. Initial state is axisymmetric. (a) Below $S < S_c = 7.2{\times}10^4$ the flow remains axisymmetric, above $S > S_c$ the flow becomes three-dimensional. This bifurcation is illustrated using the kinetic energy carried by the azimuthal component $K_{\rm tor}$ as proxy for three-dimensionality. Notice the decay or amplification for large times. (b) Simulation done with $S = 10^6$. The energy measures show that three-dimensionality comes along with nonstationarity. Notice that the total kinetic energy $K_{\rm tot}$ is higher in the three-dimensional regime than in the axisymmetric regime (i.e., for $t < 0.04$ when non-axisymmetric perturbations are negligible).

$S/10^5$	$K_{\rm tot}/10^5$	$K_{\rm axi}/10^5$	$(K_{\rm tot} - K_{\rm axi})/K_{\rm tot}$ [%]
3	8.186	7.783	4.90
4	11.10	10.42	6.19
5	14.45	13.07	9.56
10	28.48	24.90	12.6

TABLE I: Time-averaged values of the kinetic energy $K_{\rm tot}$, axisymmetric kinetic energy $K_{\rm axi}$ and ratio $(K_{\rm tot} - K_{\rm axi})/K_{\rm tot}$.

Three-dimensionality is progressively more important as S increases, but it never becomes very strong in the range of values of S we have explored. The weakness of the three-dimensional effects is visible in Figure 9(b), where we show the time evolution of $K_{\rm tor}, K_{\rm axi}, K_{\rm tot}$ at $S = 10^6$. Table I further illustrates this observation; this table gathers some numerical measures for time-averaged values of $K_{\rm tot}$ and $(K_{\rm tot} - K_{\rm axi})/K_{\rm tot}$ in the three-dimensional regime. At the highest value of S we have explored, only 12.6% of the kinetic energy is being carried by non-axisymmetric modes.

In Figure 10-(a), we show a snapshot of the typical three-dimensional flow structure at $S = 3{\times}10^5$. The flow is predominantly axisymmetric, but we observe some weak azimuthal deviations in the streamlines. Figure 10-(b) displays the maximal flow intensity and compares the 3D simulations with axisymmetric simulations. In the low S regime, the flow remains axisymmetric and nothing changes. At high S, the scaling law $u_{\rm max} \sim \sqrt{S}$ observed in the axisymmetric simulations remains valid. Three-dimensionality slightly increases the flow's intensity but this is not visible in the logarithmic plot.

D. Conclusion

The code SFEMaNS reproduces well all the quantitative and qualitative aspects of the electro-vortex flow that were previously known in the literature. The effect of a solid wire that brings the current to the liquid can be modeled correctly by using the uniform boundary condition provided the conductivity of the wire is small compared to that of the fluid. The Millere boundary condition is well suited if the conductivity of the wire is large compared to that of the fluid. The magnitude of the Lorentz force is very sensitive to the conductivity of the wire, but the component of the Lorentz force that effectively drives the electro-vortex flow is not. The electro-vortex flow predominantly remains axisymmetric up to very high values of S, and the usual low and high S scaling laws for the flow's intensity, or Reynolds number, remain valid in three-dimensional simulations and as long as the magnetic Reynolds number remains small compared to unity.

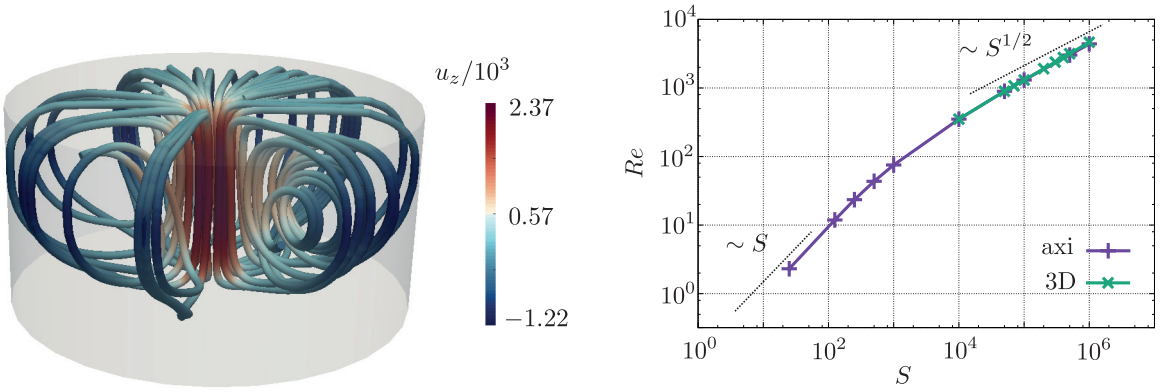

(a) (b)

FIG. 10: (a) Snapshot showing streamlines of the three-dimensional electro-vortex flow ($\hat{\sigma} = 56$, $P_\mathrm{m} = 1.57 \cdot 10^{-7}$, $S = 3 \times 10^5$). (b) Maximal flow velocity as a function of S: comparison of 3D and axisymmetric simulations.

III. ELECTRO-VORTEX FLOW IN MULTIPHASE SETUPS

After having characterized the electro-vortex flow inside a single fluid layer, we now continue with the more complex case where the fluid is composed of multiple layers. First we investigate a two layer configuration, then we investigate a three layer configuration similar to that of a Mg-Sb liquid metal battery. The calculations are done using the multiphase version of SFEMaNS and in dimensional units. The necessary information about the numerical method and equations that are solved is provided in [24]; a short summary is given in Appendix A. Since the electro-vortex flow seems to be predominantly axisymmetric, all the multiphase results reported below are obtained assuming axisymmetry.

A. Two layer setup

The two layer setup under consideration in this section is sketched in Figure 11-(a). A homogeneous current density $\boldsymbol{J}_\mathrm{bot} = (I/\pi R_w^2)\boldsymbol{e}_z$ is fed to a copper wire of length $H_w = 5\,\mathrm{cm}$, radius $R_w = 1\,\mathrm{cm}$, and conductivity $\sigma_w = 58.1{\times}10^6\,\mathrm{S\ m^{-1}}$. The radius of the fluid domain is $R = 5$ cm and there are two layers of superposed fluids. The height of the top layer is $H_1 = 1\,\mathrm{cm}$ and that of the bottom layer is $H_2 = 5\,\mathrm{cm}$. We consider two cases for the density of the top layer $\rho_1 \in \{3400, 3000\}\mathrm{kgm}^{-3}$, the density of the bottom layer is $\rho_2 = 3500\,\mathrm{kg\ m^{-3}}$. We suppose that the kinematic viscosities of the two layers are equal $\nu_1 = \nu_2 = 6.7{\times}10^{-7}\,\mathrm{m^2\ s^{-1}}$. The electrical conductivity of the top layer is $\sigma_1 = 10^4\,\mathrm{S\ m^{-1}}$ and that of the bottom layer is $\sigma_2 = 10^6\,\mathrm{S\ m^{-1}}$. The top layer has a significantly weaker conductivity than the bottom layer to mimic the situation that one encounters when in presence of a well-conducting heavy liquid metal and a badly-conducting lighter electrolyte. The current leaves the top layer uniformly $\boldsymbol{J}_\mathrm{top} = (I/\pi R^2)\boldsymbol{e}_z$. Gravity acts downwards, and we use $g = 9.81\,\mathrm{m\ s^{-2}}$.

Considering the geometry of this setup, it is mainly in the bottom layer that the electrical current spreads out. As a result, we expect the EVF phenomenon to occur in the bottom layer, and we expect the fluid in the top layer to be put in motion by viscous effects.

We start by considering the two layer setup with $\rho_1 = 3400\ \mathrm{kg\ m^{-3}}$ and a current of $I = 100\,\mathrm{A}$ is driven through the cell. This gives $S = \mu_0 I^2/(4\pi^2\rho_2\nu_2^2) = 2{\times}10^5$ in the bottom layer. The numerical simulations show that after an initial transient, the flow settles in a quasi-stationary state very similar to what we have observed in §II with one fluid layer for large values of S. Figures 11-(b) and (c) show snapshots of the intensity of the electro-vortex flow and of the density field. The EVF slightly pushes the top fluid layer upwards and deforms the interface. A weak flow is generated in the top layer as a reaction to the viscous constraints occurring at the interface. No horizontal gravity waves are observed.

We now perform a more systematic series of calculations. We consider the two cases $\rho_1 \in \{3400, 3000\}\mathrm{kg\ m^{-3}}$ and we vary the current I in the range $[100\,\mathrm{A}, 200\,\mathrm{A}]$. The nondimensional quantity S spans the interval $[2{\times}10^5, 8{\times}10^5]$. Since S is very large we posit that the scaling law $Re \sim \sqrt{S}$ is likely to apply in the bottom layer; hence in dimensional form we should have

$$U_\mathrm{max} \sim \frac{\sqrt{\mu_0} I}{\sqrt{\rho_2} R}. \tag{17}$$

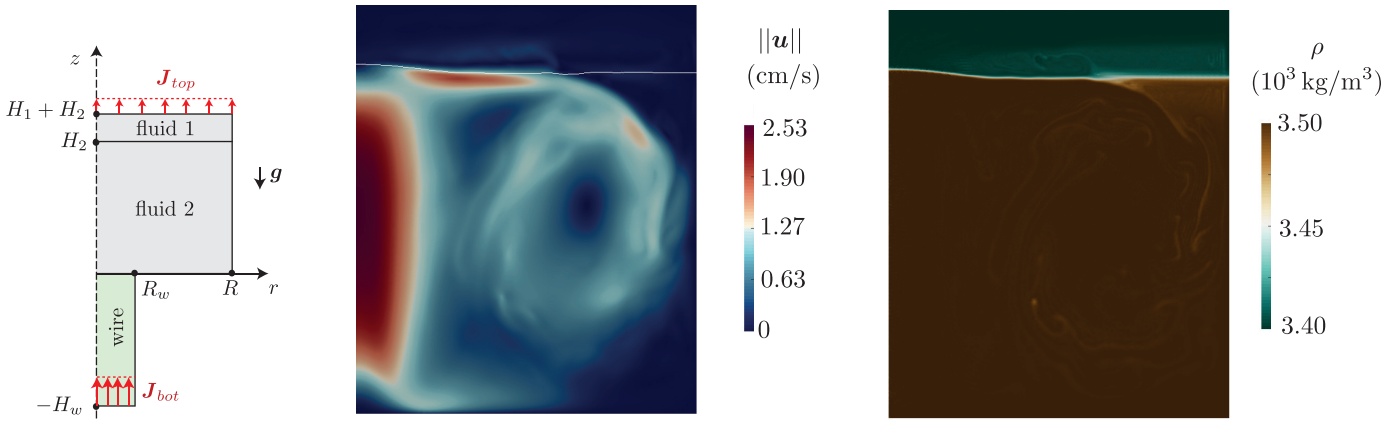

(a) two layer setup (b) flow intensity (c) density

FIG. 11: Electro-vortex flow in a two layer setup in a small cell with radius $R = 5\,\text{cm}$, wire radius $R_w = 1\,\text{cm}$, heights $H_1 = 1\,\text{cm}, H_2 = 5\,\text{cm}, H_w = 5\,\text{cm}$, current $I = 100\,\text{A}$ and densities $\rho_1 = 3400\,\text{kg m}^{-3}, \rho_2 = 3500\,\text{kg m}^{-3}$ (a) Sketch of the setup. (b) Snapshot of the electro-vortex flow. (c) Density field.

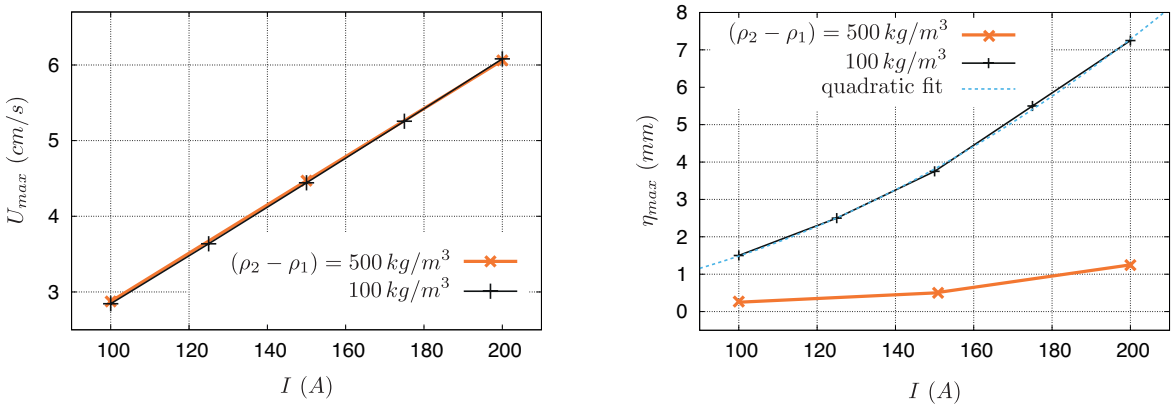

(a) (b)

FIG. 12: Variation of the maximal flow speed $U_{\max}$ (a) and the maximal interface elevation $\eta_{\max}$ (b) with current I in the two layer setup with $(R, R_w, H_1, H_2, H_w) = (5, 1, 1, 5, 5)\,\text{cm}$ and using two different density jumps $\rho_2 - \rho_1 \in \{100, 500\}\text{kg/m}^3$.

We show in Figure 12-(a) the quantity $U_{\max}$ (estimated numerically with SFEMaNS) as a function of I for the two densities $\rho_1 \in \{3400, 3000\}\text{kg m}^{-3}$. The proportionality of $U_{\max} \sim I$ is clearly visible on the graphs. Since the two curves almost coincide, this test shows that the density of the top layer, ρ_1, has very little impact on $U_{\max}$. We show in Figure 12-(b) the maximal elevation of the interface, $\eta_{\max}$, caused by the electro-vortex flow, as a function of I. The curves are well approximated by parabolas. This can be explained by balancing the available kinetic energy density in the bottom layer $\rho_2 U_{\max}^2/2$ with the potential energy density $(\rho_2 - \rho_1) g \eta_{\max}$ required to deform the interface:

$$\eta_{\max} \approx \frac{\rho_2 U_{\max}^2}{2(\rho_2 - \rho_1) g} \quad \xrightarrow{\text{eq. (17)}} \quad \eta_{\max} \approx \frac{\mu_0 I^2}{2(\rho_2 - \rho_1) g R^2}. \tag{18}$$

This suggests that the maximal surface elevation varies likes I^2 and only depends on the density difference. In non-dimensional form, this suggests

$$R_{\text{i}} = \frac{2(\rho_2 - \rho_1) g \eta_{\max}}{\rho_2 U_{\max}^2} \approx 1. \tag{19}$$

For all the simulations reported in Figure 12, we have measured $R_{\text{i}} = 1.05 \pm 0.05 \approx 1$ (data not shown). This observation implies that the above criterium (or equation (18)) makes sense as a simple formula to estimate $\eta_{\max}$.

B. Three layer setup: liquid metal battery

We now consider a three layer setup typical for a Mg-Sb liquid metal battery [1]. A sketch of the simulated system is shown in Figure 13. We fix the radius to be $R = 5\,\mathrm{cm}$ and the heights of three layers to be $(H_1, H_2, H_3) = (5, 1, 5)\,\mathrm{cm}$. Both solid electrodes have radii $R_w = 1\,\mathrm{cm}$ and have height $H_w = 5\,\mathrm{cm}$. A homogeneous current density enters the fluid bath through the bottom electrode and exits through the top electrode. The top and bottom fluid layers are composed of liquid metals, one light (fluid 1: Mg) and one heavy (fluid 3: Sb, which alloys with Mg). The layer in between is an electrolyte (fluid 2: molten salt (KCl-$MgCl_2$-NaCl)). The densities of the three fluids are chosen to make the system stable under gravity. The material parameters for the three different fluids used in our simulations, are given in Table II.

Fluid	ρ_i [kg m^{-3}]	$\rho_i\nu_i$ [Pa s]	σ_i [S m^{-1}]	$P_{\mathrm{m}i}$
1 (Mg)	1.577×10^{3}	1.23×10^{-3}	3.57×10^{6}	3.499×10^{-6}
2 (KCl-$MgCl_2$-NaCl)	1.715×10^{3}	1.40×10^{-3}	(2.56×10^{4})	2.626×10^{-8}
3 (Sb)	6.270×10^{3}	1.30×10^{-3}	2.56×10^{6}	6.670×10^{-7}

TABLE II: Density ρ_i, dynamic viscosity $\rho_i\nu_i$, conductivity σ_i and magnetic Prandtl number $P_{\mathrm{m}i}$ of the three fluids $i = 1, 2, 3$ composing a Mg-Sb liquid metal battery [11]. All values are realistic, except for σ_2 that is relaxed to $\sigma_2 = \sigma_3/100$ in order to have an improved numerical stability.

Considering the geometry of the electrodes, we expect the EVF to occur in the top and the bottom layers. High values of S are obtained in both layers when the current intensity I is in the range $[100, 300]\,\mathrm{A}$. As in the two layer setup, the fluid composing the electrolyte layer is only entrained by viscosity; therefore, we expect the motion of the fluid to be weak in this layer. Since the electrolyte is passive and the dynamic of the whole system depends very little on the conductivity of the electrolyte, in order to reduce the numerical stiffness of the problem we artificially increase the conductivity of the electrolyte by setting $\sigma_2 = \sigma_3/100$ (see Table II). This weaker conductivity jump is easier to simulate numerically and was observed not to affect the dynamic of the EVF.

We show in Figure (13)-(b) and (c) snapshots of the flow and the density field with the current $I = 200\,\mathrm{A}$. The snapshot is taken at the time $t = 20\,\mathrm{s}$ with the fluid being at rest at $t = 0$. The flow in the top layer is (somewhat surprisingly) more intense than in the bottom layer. But, following (17), we expect $U_{\max} \sim \sqrt{\mu_0}I/\sqrt{\rho_i}R$, $i = 1, 3$, in the top and the bottom layers; hence, recalling that $\frac{\rho_1}{\rho_3} \sim \frac{1}{4}$, the above formula suggests that the fluid motion in the top layer should be approximately 2 times faster than the fluid motion in the bottom layer. We also observe the interface between the top layer and the electrolyte, henceforth denoted 1|2, undergoes very large deformations while the interface between the electrolyte and the bottom layer, henceforth denoted 2|3, remains almost flat. This is mainly due to the fact that the density jump across the 1|2 interface is weak ($\rho_2 - \rho_1 = 138\,\mathrm{kgm}^{-3}$ and $\frac{\rho_2-\rho_1}{\rho_1} \sim 0.08$), whereas the density jump across the 2|3 is large ($\rho_3 - \rho_2 = 4555\,\mathrm{kgm}^{-3}$ and $\frac{\rho_3-\rho_2}{\rho_3} = 0.75$). According to (18) the maximum deformation $\eta_{\max}$ on the 1|2 interface can approximately be $\frac{4555}{138} \sim 33$ times larger than that on the 2|3 interface.

At $I = 200\,\mathrm{A}$ the interface deformation is very large, but with an even more intense current, $I = 300\,\mathrm{A}$, we find that the electro-vortex flow is so vigorous that it can cause the electrolyte layer to pinch, thereby creating a short-circuit between the two metallic phases. This situation must be avoided in real LMBs because the cell potential is lost and violent chemical reactions may make the cell unsafe. Figure 14 shows six snapshots of this simulated electrolyte pinch. The time between each picture is 0.75 s and the simulation started from rest. The downward jet in the upper layer hits the 2|3 interface violently, causing electrolyte to splash into the top layer. In the last picture, the deformed interface resembles a hydraulic jump. We recall here that that three-dimensional and the capillarity effects are not simulated. These effects would very likely modify the flow, but we are confident that the initial stage of the splashing is well captured by our axisymmetric numerical simulation.

We show in Figure 15-(a) some measures of the maximal flow speed $U_{\max}$ and of the deformation of the top interface $\eta_{\max}$ for currents in the range $I \in [100, 300]\,\mathrm{A}$. We observe the same linear and quadratic laws as in the two layer setup. The last data point for $\eta_{\max}$ at $I = 300\,\mathrm{A}$ clearly deviates from the quadratic fit because the electrolyte pinches.

We now remap the data in non-dimensional form using the definitions

$$\Pi = \frac{\sqrt{\rho_1}RU_{\max}}{\sqrt{\mu_0}I}, \qquad R_{\mathrm{i}} = \frac{2(\rho_2 - \rho_1)g\eta_{\max}}{\rho_1 U_{\max}^2}, \tag{20}$$

and show in Figure 15-(b) Π and R_{i} as functions of $S := \frac{\mu_0 I^2}{4\pi^2\rho_1\nu_1^2}$. The two non-dimensional parameters Π and R_{i} vary weakly with respect to S and they are both of order 1. The number Π seems to tend towards the asymptotic value

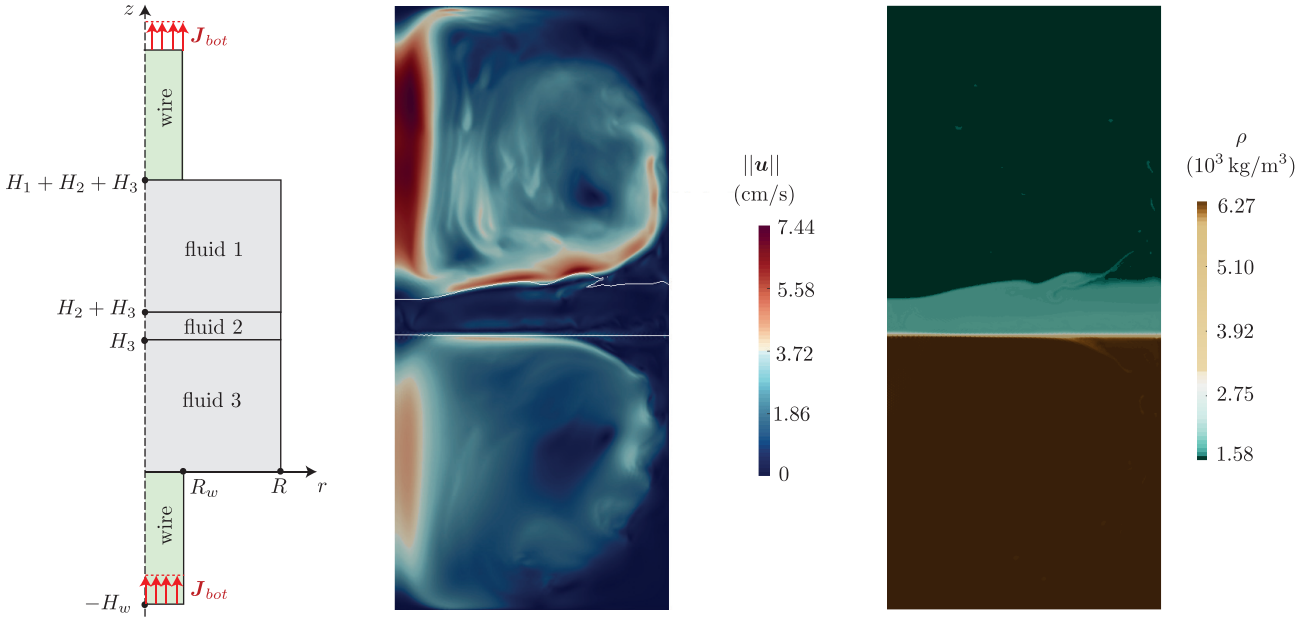

(a) setup (b) flow (c) density

FIG. 13: Electro-vortex flow in a three layer setup similar to a Mg-Sb liquid metal battery. Small cell with radius $R = 5\,\text{cm}$, wire radius $R_w = 1\,\text{cm}$, heights $(H_1, H_2, H_3, H_w) = (5, 1, 5, 5)\,\text{cm}$, current $I = 200\,\text{A}$ and densities $(\rho_1, \rho_2, \rho_3) = (1577, 1715, 6270)\,\text{kg m}^{-3}$. (a) Sketch of the setup. (b) Snapshot of the electro-vortex flow. (c) Density field.

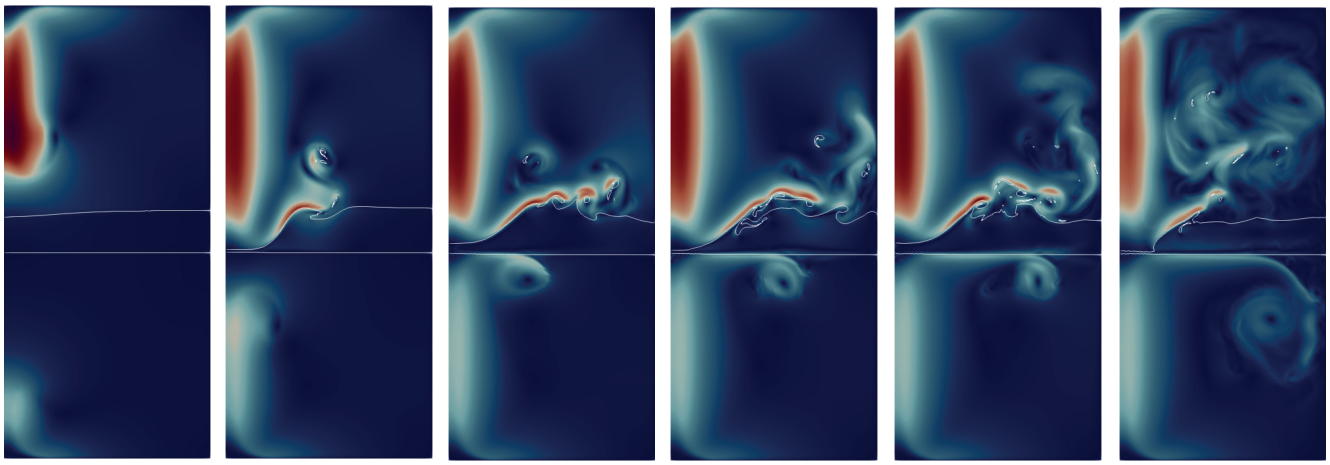

FIG. 14: When the electro-vortex flow in a Mg-Sb battery becomes too intense, it can make the electrolyte layer to pinch. In the cell considered here, this occurs at $I = 300\,\text{A}$. Starting from rest at $t = 0\,\text{s}$, we show six snapshots of the flow intensity and the interfaces at times $t = i\Delta t$, $i =\in \{1, \ldots, 6\}$ with $\Delta t = 0.75\,\text{s}$.

0.86 ± 0.01 when S becomes very large. As in the two layer setup, we observe that $R_\text{i} \gtrapprox 1$ in all the non-pinching configurations.

Using the principle of similitude, we use the data obtained above to make some predictions for upscaled Mg-Sb cells composed of the same materials and with the same geometrical aspect ratios as above. Dimensional variables without bars, $R, U_\text{max}, \eta_\text{max}, \ldots$, correspond to the previously mentioned *reference* setup. Variables with bars, $\overline{R}, \overline{U}_\text{max}, \overline{\eta}_\text{max}, \ldots$, correspond to *similar* setups. As in [11], we want to take into account that the electrical current density is bounded from above by physical limits on the mass transfer between the electrolyte and the alloy in the bottom layer [2, 4]. In the reference setup, the current density $\boldsymbol{J} \approx J\boldsymbol{e}_z$ is approximately homogeneous with $J = I/\pi R^2 \in [12.7, 38.1]\,\text{kA m}^{-2}$ for $I \in [100, 300]\,\text{A}$. These values for J are above what can be reached in existing Mg-Sb LMBs. Therefore, we consider three scenarios $\overline{J} \in \{1, 3, 10\}\,\text{kA m}^{-2}$ in the *similar* setups. The first two values are realistic for Mg-Sb batteries [1, 4], on the other hand $10\,\text{kA m}^{-2}$ is closer to what can be reached in Li-Sb(Pb)

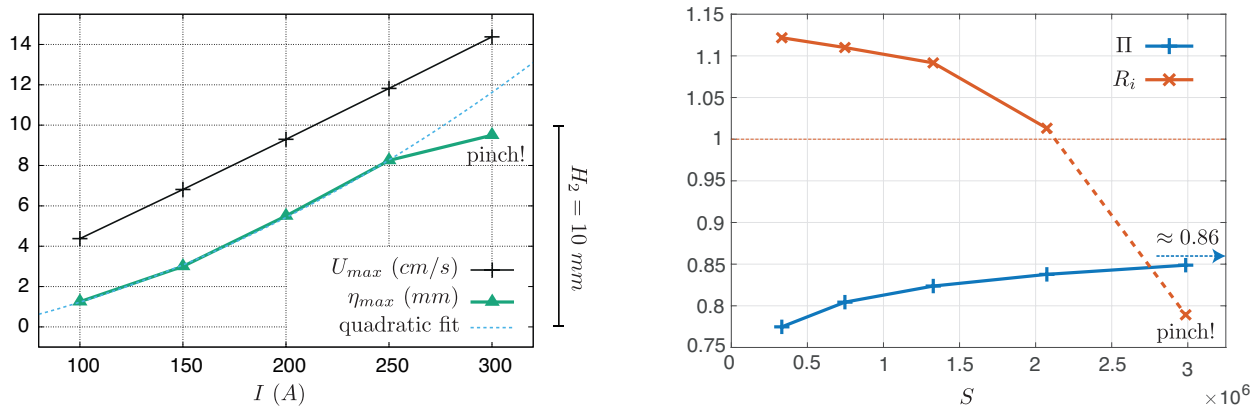

(a) (b)

FIG. 15: (a) Maximal flow intensity $U_{\max}$ and upper interface deformation $\eta_{\max}$ as a function of I in a Mg-Sb battery with dimensions $(R, R_w, H_1, H_2, H_3, H_w) = (5, 1, 5, 1, 5, 5)$ cm. We observe $U_{\max} \sim I$ and $\eta_{\max} \sim I^2$. At the highest current $I = 300$ A we observe a pinch: $\eta_{\max} \approx H_2$. (b) Non-dimensional parameters Π and R_i as a function of S using the data in (a) (see Eq. 20).

cells [3]. Requiring similitude on S (or electrical current I) implies $I = \overline{I}$, which gives I as a function of $\overline{R}$:

$$I(\overline{R}) = \pi \overline{J}\, \overline{R}^2. \tag{21}$$

Requiring similitude on the number Π (or Reynolds number Re) implies that $\overline{U}_{\max} = U_{\max}\frac{R}{\overline{R}}$. Since $U_{\max}$ is a function of I, we infer the dependency of $\overline{U}_{\max}$ with respect of $\overline{R}$ as follows:

$$\overline{U}_{\max}(\overline{R}) = U_{\max}(I(\overline{R}))\frac{R}{\overline{R}}. \tag{22}$$

Requiring similitude on R_i implies that $\overline{\eta}_{\max} = \eta_{\max}\frac{\overline{U}^2_{\max}}{U^2_{\max}} = \eta_{\max}\frac{R^2}{\overline{R}^2}$. Since $\eta_{\max}$ is a function of I, we can express $\overline{\eta}_{\max}$ as a function of $\overline{R}$ as follows:

$$\overline{\eta}_{\max}(\overline{R}) = \eta_{\max}(I(\overline{R}))\frac{R^2}{\overline{R}^2}. \tag{23}$$

The two functions $\overline{U}_{\max}(\overline{R})$ and $\overline{\eta}_{\max}(\overline{R})$ are displayed in Figure 16 for the three scenarios $\overline{J} \in \{1, 3, 10\}$ kA m^{-2}. Since we observed that $U_{\max}$ is approximately linear with respect to I, say $U_{\max} \approx \alpha I$, we infer that $\overline{U}_{\max}(\overline{R}) \approx \alpha\pi\overline{J}R\overline{R}$, i.e., $\overline{U}_{\max}$ is also approximately linear with respect to $\overline{R}$. Similarly, using that $\eta_{\max} \approx \beta I^2$, we infer that $\overline{\eta}_{\max}(\overline{R}) \approx \beta\pi^2\overline{J}^2R^2\overline{R}^2$, i.e., $\overline{\eta}_{\max}$ is also approximately quadratic in $\overline{R}$. Notice that the slope for $\overline{U}_{\max}$ behaves like $\overline{J}$ and the upward curvature of $\overline{\eta}_{\max}$ behaves like $\overline{J}^2$.

The plots of Figure 16 were made supposing perfect similitude between the *reference* and the *similar* setups, but the exact similitude constraint can be relaxed. The geometrical similitudes $R_w/R = \overline{R}_w/\overline{R} = 0.2$ and $H_1/R = \overline{H}_1/\overline{R} = 1$ directly affects the intensity of the flow in the top layer and cannot be relaxed. However, we conjecture that we should get almost the same curves as in Figure 16 if the aspect ratios of the electrolyte layer are not similar, i.e., $\frac{\overline{H}_2}{\overline{R}} \neq \frac{H_2}{R}$. This conjecture is based on the fact that a change in $\overline{H}_2$ is likely not to affect the current density distribution in the upper layer, which we recall is the source of the EVF flow. Let us reinterpret the $\overline{\eta}_{\max}$ diagram in Figure 16-(b) in this context, and let us suppose that the electrolyte has a realistic height $\overline{H_2} \in [1, 5]$ mm. Then, the EVF is probably not strong enough to pinch the electrolyte in the cell when $\overline{\eta}_{\max}$ is below 1 mm (in the green band). There is a risk of short-circuits induced by the EVF when $\overline{\eta}_{\max} \in [1, 5]$ mm (in the yellow band). Finally, it is very likely that the EVF is strong enough to make the electrolyte layer to pinch when $\overline{\eta}_{\max} > 5$ mm (in the red band). Overall, it seems from this diagram that the EVF phenomenon needs to be accounted for in the design of LMBs. Intense flows may occur in small size batteries and the risk of flow-induced short-circuits is real.

IV. CONCLUSION

The electro-vortex flow is a well known magnetohydrodynamical phenomenon that occurs near every thin electrode that is connected to a liquid metal [22]. With the numerical code SFEMaNS, we have done axisymmetric and non-axisymmetric simulations of the EVF in cylindrical fluid domains. We have explored configurations composed of one

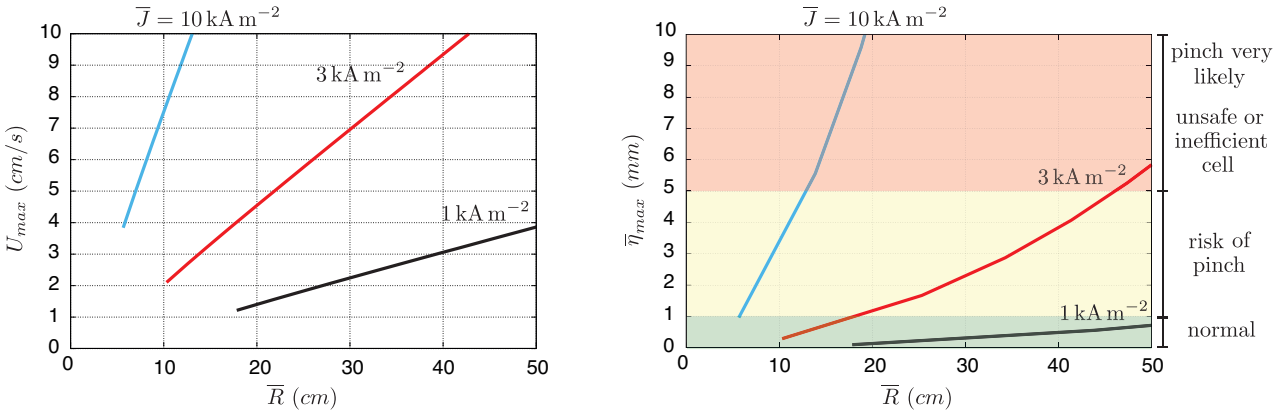

(a) (b)

FIG. 16: Using the principle of similitude we calculate the maximal flow-speed $\overline{U}_{\max}$ (panel a) and the maximal interface elevation $\overline{\eta}_{\max}$ (panel b) in similar Mg-Sb liquid metal batteries as a function of their radius $\overline{R}$ for the current density $\overline{J} \in \{1, 3, 10\}\,\mathrm{kA\ m^{-2}}$. Assuming that the dependence with respect to the height of the electrolyte layer, $\overline{H}_2$, is small and taking $\overline{H}_2 \in [1, 5]\,\mathrm{mm}$, we divide the diagram for $\overline{\eta}_{\max}$ into three regions. No risk of pinch by EVF when $\overline{\eta}_{\max} < 1\mathrm{mm}$ (green zone). Risk of pinch by EVF when $\overline{\eta}_{\max} < 1\mathrm{mm}$ (yellow zone). EVF-induced pinch very likely when $\overline{\eta}_{\max} \in [1, 5]\mathrm{mm}$ (red zone).

liquid metal and configurations composed of two and three layers with multiphase setups similar to those in liquid metal batteries.

In the single fluid layer study, we have reproduced several well known features of the electro-vortex flow, namely the flow structure and the scaling laws for the flow's intensity. The impact of the solid electrode carrying the electrical current to the cell can be modeled by using simplified boundary conditions when the wire's conductivity is either significantly larger (Millere boundary condition) or significantly smaller (uniform boundary condition) than that of the liquid metal. Three-dimensional simulations of the EVF for high values of S show that the flow is time-dependent but is also strongly dominated by its axisymmetric component.

In the multiphase study we have considered the EVF phenomenon in cells with either two or three layers of conducting fluids that are stably stratified by gravity. The EVF is generated in the vicinity of the contact between the solid electrodes and the liquid metals. The flow has roughly the same structure and intensity as in single fluid layers. The interfaces between the different phases are deformed by the flow. A simple energy density balance yields a reasonable estimate of the maximal deformation of the interface. When using the material properties of Mg-Sb liquid metal batteries, we have shown that the electro-vortex phenomenon cannot be ignored. Already in moderate size batteries it seems possible to have flows that are sufficiently intense to pinch the thin electrolyte layer. Compared to thermal convection [4–6, 8], the Tayler instability [9–11] and the metal pad roll instability [12–19], this study suggests that the electro-vortex can produce a fluid flow capable of disrupting the integrity of the upper interface.

In the future, we plan to explore whether the electro-vortex flow in liquid metal batteries could be a useful ally in order to overcome the limitations on the current density. As in all galvanic batteries, transport of charge (current) comes along with a transport of mass between the top and the bottom metal across the electrolyte. But when intense currents are extracted from (or delivered to) the cell, the alloy may become quite inhomogeneous near the alloy-electrolyte interface. This causes the battery to lose its potential or may even trigger the appearance of undesirable solid inter-metallic phases. Just as natural convection [4], the electro-vortex flow has the capacity to mix the bottom alloy [7, 20] and we need to asses if this is indeed possible or not.

Acknowledgments

The HPC resources were provided by GENCI-IDRIS (grant 2018-0254) in France and by the Texas A&M University Brazos HPC cluster. J.-L. Guermond acknowledges support from Univ. Paris Sud, the National Science Foundation, under grants NSF DMS 1620058, DMS 1619892, the Air Force Office of Scientific Research, USAF, under grant/contract number FA9550-18-1-0397, and the Army Research Office under grant/contract number W911NF-15-1-0517. This work was supported by the Deutsche Forschungsgemeinschaft (DFG, German Research Foundation) under award number 338560565. L. Cappanera is thankful to Texas A&M University, LIMSI, and CNRS for their financial support.

Appendix A: Some extra information on our numerical code SFEMaNS

For solving the system of equations (5) we use SFEMaNS (the acronym stands for Spectral/Finite Element code for Maxwell and Navier-Stokes equations). We use a Fourier decomposition in the azimuthal θ-direction and continuous finite elements in the meridian section ($\mathbb{P}_1$ Lagrange elements for the pressure and $\mathbb{P}_2$ Lagrange elements for the velocity and the magnetic field). For instance the approximate velocity field has the following representation:

$$\mathbf{u} = \sum_{m=0}^{M-1} \mathbf{u}_m^c(r,z,t)\cos(m\theta) + \sum_{m=1}^{M-1} \mathbf{u}_m^s(r,z,t)\sin(m\theta), \tag{A1}$$

where $\mathbf{u}_m^c(r,z,t)$ and $\mathbf{u}_m^s(r,z,t)$ are vector-valued finite elements functions and M is the number of (complex) Fourier mode used in the discretization. All the fields, either vector-valued or scalar-valued, are represented as above. Modulo the computation of nonlinear terms using FFT3W, the handling of the Fourier modes in the meridian plane, (r,z), can be done in parallel. The divergence of $\mathbf{b}$ is controlled by a technique using a negative Sobolev norm that guarantees convergence under minimal regularity (see details in [34], [35, §3.2], [36]). SFEMaNS has been thoroughly validated on numerous manufactured solutions and against other magnetohydrodynamics codes (see e.g. [37, 38]).

Liquid metal batteries include more than one fluid. The presence of multiple phases is accounted for in SFEMaNS by using a level set technique. Denoting by ρ, $\mathbf{m} = \rho\mathbf{u}$, p and $\mathbf{b}$ the density, the momentum, the pressure and the magnetic field, respectively, the conservation of mass, the conservation of momentum, the solenoidality of the magnetic field, and the induction equation are expressed as follows in dimensional units:

$$\partial_t \rho + \boldsymbol{\nabla}\cdot\mathbf{m} = 0, \tag{A2a}$$

$$\boldsymbol{\nabla}\cdot\mathbf{u} = 0, \tag{A2b}$$

$$\partial_t \mathbf{m} + \boldsymbol{\nabla}\cdot(\mathbf{m}\otimes\mathbf{u}) - \boldsymbol{\nabla}\cdot(\eta(\boldsymbol{\nabla}\mathbf{u} + (\boldsymbol{\nabla}\mathbf{u})^T)) + \boldsymbol{\nabla}p = -\rho g \boldsymbol{e}_z + \frac{(\boldsymbol{\nabla}\times\mathbf{b})\times\mathbf{b}}{\mu_0}, \tag{A2c}$$

$$\boldsymbol{\nabla}\cdot(\mathbf{b}) = 0, \tag{A2d}$$

$$\partial_t \mathbf{b} + \boldsymbol{\nabla}\times\left(\frac{\boldsymbol{\nabla}\times\mathbf{b}}{\mu_0\sigma}\right) = \boldsymbol{\nabla}\times(\mathbf{u}\times\mathbf{b}), \tag{A2e}$$

where the density ρ, the dynamic viscosity η and the electrical resistivity $1/\sigma$ are reconstructed by means of level set functions [24]. For example, in the two layer case, the density is given by $\rho = \rho_2 + (\rho_1 - \rho_2)\phi = \rho_2(1-\phi) + \rho_1\phi$ with the sharply varying level set function $\phi \in [0,1]$. In the three layer case, two level set functions are used such that, e.g. $\rho_{21}(\phi_1) = \rho_2(1-\phi_1) + \rho_1\phi_1$ and $\rho = \rho_3(1-\phi_2) + \rho_{21}(\phi_1)\phi_2$, where $\phi_1 \in [0,1]$ varies steeply across the interface between the top layer (1) and the electrolyte (2), and $\phi_2 \in [0,1]$ varies sharply across the interface between the electrolyte (2) and the bottom layer (3). The term $-\rho g \boldsymbol{e}_z$ is the buoyancy force; the unit vector $\boldsymbol{e}_z$ conventionally gives the upward direction.

[1] David J. Bradwell, Hojong Kim, Aislinn H.C. Sirk, and Donald R. Sadoway. Magnesium–antimony liquid metal battery for stationary energy storage. *Journal of the American Chemical Society*, 134(4):1895–1897, 2012.

[2] H. Kim, D. A. Boysen, T. Ouchi, and D.R. Sadoway. Calcium–bismuth electrodes for large-scale energy storage (liquid metal batteries). *Journal of Power Sources*, 241:239–248, 2013.

[3] Kangli Wang, Kai Jiang, Brice Chung, Takanari Ouchi, Paul J. Burke, Dane A. Boysen, David J. Bradwell, Hojong Kim, Ulrich Muecke, and Donald R. Sadoway. Lithium-antimony-lead liquid metal battery for grid-level energy storage. *Nature*, 514(7522):348–350, 2014.

[4] Douglas H. Kelley and Donald R. Sadoway. Mixing in a liquid metal electrode. *Physics of Fluids*, 26(5):057102, 2014.

[5] Yuxin Shen and Oleg Zikanov. Thermal convection in a liquid metal battery. *Theor. Comput. Fluid Dyn.*, 30(4):275–294, 2016.

[6] Thomas Köllner, Thomas Boeck, and Jörg Schumacher. Thermal Rayleigh-Marangoni convection in a three-layer liquid-metal-battery model. *Phys. Rev. E*, 95:053114, May 2017.

[7] R. F. Ashour, D. H. Kelley, A. Salas, M. Starace, N. Weber, and T. Weier. Competing forces in liquid metal electrodes and batteries. *Journal of Power Sources*, 378:301–310, 2018.

[8] Paolo Personnettaz, Pascal Beckstein, Steffen Landgraf, Thomas Kllner, Michael Nimtz, Norbert Weber, and Tom Weier. Thermally driven convection in Li||Bi liquid metal batteries. *Journal of Power Sources*, 401:362–374, 2018.

[9] N. Weber, V. Galindo, F. Stefani, and T. Weier. Current-driven flow instabilities in large-scale liquid metal batteries, and how to tame them. *Journal of Power Sources*, 265(0):166–173, 2014.

[10] N. Weber, V. Galindo, J. Priede, F. Stefani, and T. Weier. The influence of current collectors on Tayler instability and electro-vortex flows in liquid metal batteries. *Physics of Fluids*, 27(1):014103, 2015.

[11] W. Herreman, C. Nore, L. Cappanera, and J.-L. Guermond. Tayler instability in liquid metal columns and liquid metal batteries. *Journal of Fluid Mechanics*, 771:79–114, 2015.

[12] O. Zikanov. Metal pad instabilities in liquid metal batteries. *Physical Review E*, 92(6):063021, 2015.

[13] N. Weber, P. Beckstein, W. Herreman, G.M. Horstmann, C. Nore, F. Stefani, and T. Weier. Sloshing instability and electrolyte layer rupture in liquid metal batteries. *Physics of Fluids*, 29(5):054101, 2017.

[14] N. Weber, P. Beckstein, V. Galindo, W. Herreman, C. Nore, F. Stefani, and T. Weier. Metal pad roll instability in liquid metal batteries. *Magnetohydrodynamics*, 53(1):129–140, 2017.

[15] V. Bojarevics and A. Tucs. MHD of large scale liquid metal batteries. In *Light Metals 2017*, pages 687–692. Springer, 2017.

[16] G. M. Horstmann, N. Weber, and T. Weier. Coupling and stability of interfacial waves in liquid metal batteries. *Journal of Fluid Mechanics*, 845:1–35, 2018.

[17] S. Molokov. The nature of interfacial instabilities in liquid metal batteries in a vertical magnetic field. *Europhysics Letters*, 121(4):44001, 2018.

[18] O. Zikanov. Shallow water modeling of rolling pad instability in liquid metal batteries. *Theoretical and Computational Fluid Dynamics*, 32(3):325–347, 2018.

[19] W. Herreman, C. Nore, J.-L. Guermond, L. Cappanera, N. Weber, and G. M. Horstmann. Metal pad roll instability in cylindrical reduction cells. *submitted to Journal of Fluid Mechanics*, 2019.

[20] N. Weber, M. Nimtz, P. Personnettaz, A. Salas, and T. Weier. Electromagnetically driven convection suitable for mass transfer enhancement in liquid metal batteries. *Applied Thermal Engineering*, 143:293–301, 2018.

[21] D. H. Kelley and T. Weier. Fluid mechanics of liquid metal batteries. *Applied Mechanics Reviews*, 70:020801, 2018.

[22] V. Bojarevics, J. A. Freibergs, E. I. Shilova, and E. V. Shcherbinin. *Electrically Induced Vortical Flows*. Kluwer Academic Publishers, 1989.

[23] J. A. Shercliff. Fluid motions due to an electric current source. *J. Fluid Mech.*, 40:241–250, 1969.

[24] L. Cappanera, J.-L. Guermond, W. Herreman, and C. Nore. Momentum-based approximation of incompressible multiphase fluid flows. *International Journal for Numerical Methods in Fluids*, 86(8):541–563, 2018.

[25] R. P. Millere, V. I. Sharamkin, and . V. Shcherbinin. Effect of a longitudinal magnetic field on electrically driven rotational flow in a cylindrical vessel. *Magnitnaya Gidrodinamika*, 1:81–85, 1980.

[26] I. E. Butsenieks, D. E. Peterson, V. I. Sharamkin, and E. V. Sherbinin. Magnetohydrodynamic fluid flows in a closed space with a nonuniform electric current. *Magn. Gidrodin.*, 1:92–97, 1976.

[27] V. K. Vlasyuk. Effects of fusible-electrode radius on the electrovortex flow in a cylindrical vessel. *Magn. Gidrodin.*, 4:101–106, 1987.

[28] A. Y. Chudnovskii. Evaluating the intensity of a single class of electrovortex flows MHD. *Magnetohydrodynamics*, 25(3):406–408, 1989.

[29] Petr A. Nikrityuk, Kerstin Eckert, Roger Grundmann, and Yuansheng S. Yang. An Impact of a Low Voltage Steady Electrical Current on the Solidification of a Binary Metal Alloy: A Numerical Study. *Steel Res. Int.*, 78(5):402–408, 2007.

[30] Christoph Kasprzyk. *Numerische Untersuchung Zur Strömungsmechanik in Flüssigmetallbatterien*. Master thesis, Technische Universität Dresden, 2015.

[31] Norbert Weber, Pascal Beckstein, Vladimir Galindo, Marco Starace, and Tom Weier. Electro-vortex flow simulation using coupled meshes. *Comput. Fluids*, 168:101–109, 2018.

[32] V. G. Zhilin, Y. P. Ivochkin, A. A. Oksman, G. R. Lurin'sh, A. I. Chaikovskii, A. Y. Chudnovskii, and E. V. Shcherbinin. An experimental investigation of the velocity field in an axisymmetric electrovortical flow in a cylindrical container. *Magn. Gidrodin.*, 3:110–116, 1986.

[33] L. A. Volokhonskii. Dynamic boundary layer of electrovortex flow in a cylindrical volume with axisymmetric current supply. *Magnetohydrodynamics*, 27(4):467–470, 1991.

[34] A. Bonito and J.-L. Guermond. Approximation of the eigenvalue problem for the time harmonic Maxwell system by continuous Lagrange finite elements. *Math. Comp.*, 80(276):1887–1910, 2011.

[35] A. Giesecke, C. Nore, F. Stefani, G. Gerbeth, J. Léorat, F. Luddens, and J.-L. Guermond. Electromagnetic induction in non-uniform domains. *Geophys. Astrophys. Fluid Dyn.*, 104(5):505–529, 2010.

[36] A. Bonito, J.-L. Guermond, and F. Luddens. Regularity of the Maxwell equations in heterogeneous media and Lipschitz domains. *Journal of Mathematical Analysis and applications*, 408(2):498–512, December 2013.

[37] J.-L. Guermond, R. Laguerre, J. Léorat, and C. Nore. Nonlinear magnetohydrodynamics in axisymmetric heterogeneous domains using a Fourier/finite element technique and an interior penalty method. *J. Comput. Phys.*, 228:2739–2757, 2009.

[38] A. Giesecke, C. Nore, F. Stefani, G. Gerbeth, J. Léorat, W. Herreman, F. Luddens, and J.-L. Guermond. Influence of high-permeability discs in an axisymmetric model of the Cadarache dynamo experiment. *New Journal of Physics*, 14(5):053005, 2012.